atmosphere

MDPI

Article

Optimal Estimation Retrieval of Aerosol Fine-Mode Fraction from Ground-Based Sky Light Measurements

Fengxun Zheng [1,2], Weizhen Hou [1,3], Xiaobing Sun [4], Zhengqiang Li [1,3,*], Jin Hong [4], Yan Ma [1], Li Li [1], Kaitao Li [1], Yizhe Fan [4] and Yanli Qiao [4]

1 State Environment Protection Key Laboratory of Satellite Remote Sensing, Institute of Remote Sensing and Digital Earth, Chinese Academy of Sciences, Beijing 100101, China; zhengfx@radi.ac.cn (F.Z.); houwz@radi.ac.cn (W.H.); mayan01@radi.ac.cn (Y.M.); liligis@163.com (L.L.); likt@radi.ac.cn (K.L.)
2 University of Chinese Academy of Sciences, Beijing 100049, China
3 State Key Laboratory of Remote Sensing Science, Institute of Remote Sensing and Digital Earth, Chinese Academy of Sciences, Beijing 100101, China
4 Key Laboratory of Optical Calibration and Characterization, Anhui Institute of Optics and Fine Mechanics, Chinese Academy of Sciences, Hefei 230031, China; xbsun@aiofm.ac.cn (X.S.); hongjin@aiofm.ac.cn (J.H.); yzfan@mail.ustc.edu.cn (Y.F.); ylqiao@aiofm.ac.cn (Y.Q.)
* Correspondence: lizq@radi.ac.cn; Tel.: +86-010-64806225

Received: 18 March 2019; Accepted: 9 April 2019; Published: 11 April 2019

Abstract: In this paper, the feasibility of retrieving the aerosol fine-mode fraction (FMF) from ground-based sky light measurements is investigated. An inversion algorithm, based on the optimal estimation (OE) theory, is presented to retrieve FMF from single-viewing multi-spectral radiance measurements and to evaluate the impact of utilization of near-infrared (NIR) measurements at a wavelength of 1610 nm in aerosol remote sensing. Self-consistency tests based on synthetic data produced a mean relative retrieval error of 4.5%, which represented the good performance of the OE inversion algorithm. The proposed algorithm was also performed on real data taken from field experiments in Beijing during a haze pollution event. The correlation coefficients (R) for the retrieved aerosol volume fine-mode fraction (FMF_v) and optical fine-mode fraction (FMF_o) against AErosol RObotic NETwork (AERONET) products were 0.94 and 0.95 respectively, and the mean residual error was 4.95%. Consequently, the inversion of FMF_v and FMF_o could be well constrained by single-viewing multi-spectral radiance measurement. In addition, by introducing measurements of 1610 nm wavelength into the retrieval, the validation results showed a significant improvement in the R value for FMF_o (from 0.89–0.94). These results confirm the high value of NIR measurements for the retrieval of coarse mode aerosols.

Keywords: aerosol optical depth; fine-mode fraction; optimal estimation inversion

1. Introduction

Exposure to ambient air pollution has serious impacts on human health, such as respiratory diseases and cardiovascular diseases [1–4]. Some of the diseases are mainly caused by atmospheric fine particulate matters ($PM_{2.5}$, more precisely, particulate matters with aerodynamic diameters less than 2.5 μm) [5,6]. Thus, the estimation of the $PM_{2.5}$ mass concentration near the surface has been extensively studied using ground-based and satellite platforms, such as the pure physical $PM_{2.5}$ remote sensing (PMRS) method [7–9]. As a parameter to describe the proportion of fine particles in aerosols, fine-mode fraction (FMF) is a key factor in the physical model, which can increase people's understanding of anthropogenic aerosols and help to analyze the impacts of human activities on environmental changes and human health [10,11].

Regarding satellite remote sensing, previous studies attempted to retrieve FMF over the dark target region from observations of the Moderate Resolution Imaging Spectroradiometer (MODIS) [12–14]. However, the accuracy of retrieved FMF was not sufficient for estimating $PM_{2.5}$ mass concentration near the ground. [15]. There are also some related algorithms that try to retrieve FMF from measurements of the multi-viewing polarized satellite sensor, such as the Polarization and Directionality of the Earth's Reflectances (POLDER) onboard the Polarization and Anisotropy of Reflectances for Atmospheric Science coupled with Observations from a Lidar (PARASOL), whereas most of the algorithms are limited to the research phase and cannot obtain stable and reliable products [16–18]. On the other hand, the optical and microphysical properties of aerosol can be derived from ground-based remote sensing measurements. The active Raman and elastic lidar techniques provide the vertical structure of cloud and aerosol properties. However, studies of aerosol optical FMF parameters resolved from multi-spectral lidar still need to be further developed [19]. With regard to the passive measurements of direct and diffused radiation, there are currently two approaches to obtain the FMF. One is using the semi-empirical method, called spectral discrimination, to calculate FMF, which is based on the high-precision spectral aerosol optical depth (AOD) from the direct measurements of a Sun Photometer [20]. The method is also the operational algorithm to get FMF products of the AErosol RObotic NETwork (AERONET) [21]. The other is obtaining physical volume concentrations of fine and coarse particles, first by scattering light measurements from the atmosphere [22], and then by calculating FMF from the results of particle size distribution (PSD). However, there are still some limitations in the latter approach, such as a lack of constraint of coarse aerosol particles without obtaining measurements of longer wavebands.

For passive instruments that detect reflected or scattered solar radiation, shortcomings are generally due to the limited information available in the measurements [23]. Consequently, both ground-based and satellite sensors, such as CE318-DP, POLDER, and DPC (Directional Polarimetric Camera), are currently focused on multi-band, multi-angle, and polarization observations to increase effective information [24–27]. However, as the instruments become more and more complex, it becomes increasingly difficult to link the aerosol parameter retrieval capability to measurement characteristics intuitively, especially for polarimetric observations. In this paper, we try to explore the possibility of spectral AOD and FMF inversion using ground-based, single-viewing, multi-spectral intensity measurements of the sky light. For this purpose, the measurement of the near-infrared (NIR) band centered on 1610 nm was introduced to improve the retrieval capability for coarse-mode aerosols [28]. At the same time, a multi-parameter inversion framework based on the optimal estimation (OE) theory [29] was adopted to make full use of the observation information.

The paper is organized as follows. Following an overview of the model and algorithm in Section 2, we introduce the ground-based field experiment data acquired by the Synchronization Monitoring Atmospheric Corrector (SMAC) sensor in Section 3. Subsequently, the retrieval algorithm is tested using the synthetic data and the real data in Section 4. A brief discussion is given in Section 5. Finally, the summary and conclusion are presented in Section 6.

2. Model and Methods

2.1. Aerosol Model

In line with many studies [30,31], a bimodal lognormal function is adopted to describe the volume PSD of spherical aerosol particles in the following form:

$$\frac{dV}{d\ln r} = \sum_{i=1}^{2} \frac{V_0^i}{\sqrt{2\pi}\ln\sigma_g^i} \exp\left[-\frac{\left(\ln r - \ln r_v^i\right)}{2\ln^2\sigma_g^i}\right], \quad (1)$$

where V is the particle volume, r is the radius, $dV/d\ln r$ represents the volume contained in each logarithmic particle size interval, r_v and σ_g represent the volume geometric median radius and the geometric standard deviation, respectively, and the superscript "i" denotes the aerosol mode; hereafter,

we use "f" and "c" to represent fine and coarse mode, respectively. Then, we get the total aerosol volume concentration V_0 (with unit of $\mu m^3 \mu m^{-2}$) from the sum of V_0^f and V_0^c. Furthermore, the fine-mode volume fraction is calculated as

$$\mathrm{FMF_v} = V_0^f / V_0. \tag{2}$$

Then, the spectral AOD is derived from the columnar volume concentration as [32]

$$\tau_a(\lambda) = \tau_a^f(\lambda) + \tau_a^c(\lambda) = \frac{3V_0^f Q_{ext}^f(\lambda)}{4r_{eff}^f} + \frac{3V_0^c Q_{ext}^c(\lambda)}{4r_{eff}^c}, \tag{3}$$

where Q_{ext} represents the aerosol extinction efficiency factor, which is defined as the ratio between the extinction cross section and the geometric cross section. Based on the hypothesis of aerosol spherical particles, Q_{ext} is calculated by the Mie code. τ_a^f and τ_a^c represent the fine-mode and coarse-mode spectral AOD respectively, and the total AOD (τ_a) is the sum of τ_a^f and τ_a^c. The effective radius (r_{eff}) and the effective variance (v_{eff}) are converted from the geometric parameters by the relationship as

$$\begin{cases} r_{eff} = r_v \exp\left(-\frac{1}{2}\ln^2\sigma_g\right) \\ v_{eff} = \exp\left(\ln^2\sigma_g\right) - 1 \end{cases}. \tag{4}$$

Correspondingly, the aerosol spectral fine-mode fraction ($\mathrm{FMF_o}$) and the Ångström exponent (AE) are calculated as

$$\mathrm{FMF_o}(\lambda) = \tau_a^f(\lambda)/\tau_a(\lambda), \tag{5}$$

$$\mathrm{AE} = \ln\frac{\tau_a(\lambda_1)}{\tau_a(\lambda_2)} / \ln\frac{\lambda_1}{\lambda_2}, \tag{6}$$

where λ_1 and λ_2 in Equation (6) represent two specific wavelengths, e.g., 670 and 865 nm.

Actually, the definition for the proportion of fine aerosols to total aerosols is not exactly in the same form. Table 1 lists the definitions of FMF used in different studies. Despite the inconsistency between these definitions, all of them can represent well the proportion of fine particles in the atmosphere. The $\mathrm{FMF_v}$ and $\mathrm{FMF_o}$ used in this paper are derived from the bimodal aerosol model and defined from the physical and optical perspectives separately.

Table 1. Definitions for the proportions of fine aerosols to total aerosols in different studies.

Abbreviation	Distinction of definition	References
FMF	The fine-mode fraction (FMF) is defined optically and calculated by the optical spectral deconvolution algorithm (SDA) rather than intermediate computations of the aerosol particle size distribution (PSD) parameters and refractive indices.	[20]
	The FMF is defined optically and retrieved independently by irrelevant aerosol model assumptions for total aerosol optical depth (AOD) and fine-mode AOD.	[11]
$\mathrm{FMF_v}$/$\mathrm{FMF_o}$	The physical volume fine-mode fraction ($\mathrm{FMF_v}$)/optical fine-mode fraction ($\mathrm{FMF_o}$) is defined based on a physical model in which the fine and coarse components follow a unified bimodal aerosol model. The subscripts 'v' and 'o' denote volume FMF and optical FMF, respectively.	[22,28,31]
SMF	The SMF (Sub Micrometer Fraction) is defined in terms of a microphysical cutoff of the associated PSD at some specific radius. Two acquisition methods are available: (1) calculating using the cutoff radius based on the bimodal aerosol model; and (2) obtaining it by in situ measurement. The widely accepted cut-off radius is 0.6μm.	[33–35]

FMF_v is a wavelength-independent physical quantity, while FMF_o varies with wavelength. The relationship between FMF_v and FMF_o is shown in Figure 1. The conversion is performed by Mie code with aerosol parameters listed in Table 2. Those aerosol model parameters are derived from the statistics of multi-year ground-based observation network inversion products [36]. The values of refractive indices in the table correspond to 490, 550, 670, 870, and 1610 nm, respectively. It can be seen from Figure 1 that there is a significantly nonlinear relationship between the two parameters, especially in visible bands. At 550 nm, FMF_o reaches up to 0.9 when the FMF_v is equal to 0.5, which means the fine particles produce significant extinction effects in the visible light band. However, for the curve of the NIR band (1610 nm), it is different from the other four curves in visible bands. The FMF_o grows relatively slowly when FMF_v is less than 0.6. The reason for this phenomenon is that the extinction effect of coarse mode aerosols improves significantly while the extinction effect of fine mode aerosols decreases in long NIR bands. In general, the relationship between FMF_v and FMF_o at 1610 nm reveals the sensitivity of longer NIR wavelengths to coarse particles.

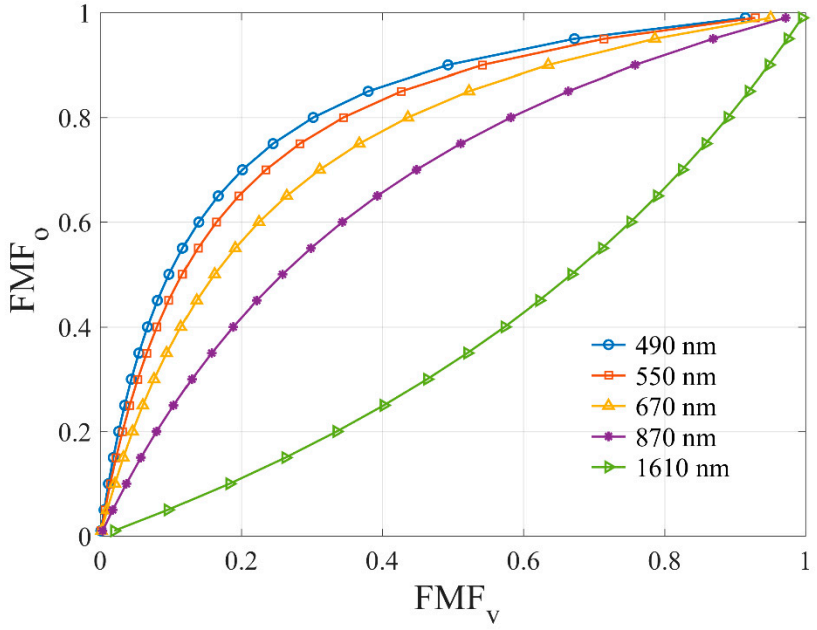

Figure 1. The relationship between aerosol spectral FMF_o and FMF_v.

Table 2. The aerosol model parameters adopted for simulation and inversion in this paper.

Mode	r_{eff} (μm)	v_{eff}	m_r	m_i
Fine	0.155	0.284	1.39, 1.40, 1.40, 1.42, 1.41	0.0079, 0.0075, 0.0066, 0.0066, 0.0067
Coarse	2.213	0.482	1.53, 1.54, 1.55, 1.54, 1.50	0.0049, 0.0041, 0.0023, 0.0019, 0.0009

2.2. Modeling for Ground-Based Observation

Generally, for the modeling of downward radiation, the uncertainty of surface reflectance can be ignored for the reason that the change in downward atmospheric radiation mainly depends on the properties of aerosols and molecule scattering [22]. Therefore, the Lambertian surface hypothesis is adopted to describe the contribution of the surface in this study. In addition, the ground-based measured radiation is mainly affected by the entire atmospheric column and is not strongly dependent on the vertical distribution of aerosols. Considering that atmospheric aerosols are usually trapped in the planetary boundary layer (PBL), we use the exponentially shaped profile distribution model and set the scale height to 2 km in this study [37,38].

With respect to the calculation of radiation transfer, the Unified Linearized Vector Radiative Transfer Model (UNL-VRTM) is employed as the forward model, which was specifically designed for

the simulation of atmospheric remote sensing observations and for the inversion of corresponding properties from these observations [39]. The outputs of UNL-VRTM include not only the four elements of the Stokes vector but also their sensitivities (Jacobians) with respect to aerosol and surface model parameters. The UNL-VRTM is widely used to develop the inversion algorithm for retrieval of aerosol and surface properties from ground-based, airborne, and satellite measurements [31,40–43].

2.3. Methodology

2.3.1. OE inversion Method

Based on the optimal estimation theory, the forward model can be described as the following formula [29]:

$$\boldsymbol{y} = \boldsymbol{F}(\boldsymbol{x}, \boldsymbol{b}) + \boldsymbol{\epsilon}, \tag{7}$$

where $\boldsymbol{y}$ is the observation vector with N_y measurement elements, $\boldsymbol{x}$ represents a state vector that contains N_a parameters to be retrieved, $\boldsymbol{b}$ means the non-state vector, including all model parameters that we do not seek to optimize, $\boldsymbol{F}$ denotes the physical process from state vector to observation vector, and $\boldsymbol{\epsilon}$ is an error term, including uncertainties contained in measurements and forward modeling.

In the presence of $\boldsymbol{\epsilon}$, the inversion result is a statistical estimate other than the exact value. Thus, under the assumption of a Gaussian distribution of errors, an inversion problem can be converted to solve the minimum value of cost function $J(\boldsymbol{x})$, which is composed of two terms, expressed as the following:

$$J(\boldsymbol{x}^p) = \frac{1}{2}[\boldsymbol{y} - \boldsymbol{F}(\boldsymbol{x}^p)]^T \boldsymbol{S}_y^{-1}[\boldsymbol{y} - \boldsymbol{F}(\boldsymbol{x}^p)] + \frac{1}{2}\gamma_a(\boldsymbol{x}^p - \boldsymbol{x}_a)^T \boldsymbol{S}_a^{-1}(\boldsymbol{x}^p - \boldsymbol{x}_a), \tag{8}$$

where the superscript "−1" represents an inversion operation and "T" represents a transpose operation; $\boldsymbol{x}_a$ describes an estimate of state vector, and $\boldsymbol{x}^p$ represents the state vector of the p-th iteration; $\boldsymbol{S}_a$ denotes the error covariance matrix for a priori estimate, and $\boldsymbol{S}_y$ is the error covariance matrix representing the uncertainty occurring in the measuring process. We use zero off-diagonal elements for $\boldsymbol{S}_y$ by assuming that errors are independent between measurements. Besides, the a priori estimate errors are also assumed to be noncorrelated, which gives a diagonal matrix of $\boldsymbol{S}_a$. Two terms in the right side of Equation (8) describe the contributions of observation and a priori estimate into the solution separately. The Lagrange multiplier γ_a is a regularization parameter, and is defined following the work of Xu et al. [31]:

$$\gamma_a = N_y / N_a. \tag{9}$$

Usually, solving the minimum value of the $J(\boldsymbol{x})$ is a nonlinear problem and always needs multiple iterations. Quasi-Newton methods are widely used for finding the local maximum and/or minimum of the nonlinear function [44,45],

$$\boldsymbol{x}^{p+1} = \boldsymbol{x}^p - \alpha_p \boldsymbol{H}_p \nabla J(\boldsymbol{x}^p)^T, \tag{10}$$

where $\boldsymbol{H}$ is the inverse matrix of the Hessian matrix constructed with successive gradient vectors in the quasi-Newton method, and α_p is the iterated step length which is chosen to minimize $J\left(\boldsymbol{x}^{p+1}\right)$. The gradient of $J(\boldsymbol{x})$ can be defined as,

$$\nabla J(\boldsymbol{x}^p) = \frac{\partial J(\boldsymbol{x}^p)}{\partial \boldsymbol{x}} = \boldsymbol{K}_p^T \boldsymbol{S}_\epsilon^{-1}[\boldsymbol{F}(\boldsymbol{x}^p) - \boldsymbol{y}] + \gamma_a \boldsymbol{S}_a^{-1}(\boldsymbol{x}^p - \boldsymbol{x}_a), \tag{11}$$

where $\boldsymbol{K}$ is the Jacobians matrix of $\boldsymbol{F}(\boldsymbol{x})$ with respect to $\boldsymbol{x}$, and $\boldsymbol{K} = \frac{\partial \boldsymbol{F}(x)}{\partial \boldsymbol{x}}$. The sensitivity of radiance with respect to the aerosol microphysical parameters can be calculated by UNL-VRTM. The second term in the right side of Equation (11) describes the convergence direction and step length of the state vector from the p-th iteration and (p + 1)-th iteration. We perform an iterative Quasi-Newton approach using the L-BFGS-B algorithm to find the minimization of $J(\boldsymbol{x})$ [46–48]. The L-BFGS-B algorithm is a highly effective tool in bounded minimization problems with the requirements of a priori knowledge,

cost function, and the gradient of the cost function. When the results after multiple iterations satisfy the condition of $\|\boldsymbol{x}^{p+1} - \boldsymbol{x}^{p}\| \leq \varepsilon$, the iterative process is terminated, and an optimized estimate of $\boldsymbol{x}$ is obtained, where ε is the threshold for convergence.

2.3.2. Inversion Settings

For the OE inversion framework, the first task is to determine the observation data and the state vector to be retrieved, as well as the observational uncertainties and a priori estimation error, respectively. These inversion parameter settings are listed in Table 3. The observation vector $\boldsymbol{y}$ is composed of the normalized radiance (referred to as I in Table 3) at 490, 550, 670, 870, and 1610 nm wavelengths. The level of recognized observation error is usually around 3–5% for intensity measurements, and the observation error does not vary with wavelength, observation mode, and observation geometry in this paper. The state vector $\boldsymbol{x}$ is composed of the aerosol V_0 and $\mathrm{FMF_v}$. The a priori estimate of $\boldsymbol{x}$ comes from the available inversion products of AERONET, and a relative error of 100% is adopted for the state vector during the inversion. The non-state vector $\boldsymbol{b}$ is composed of the aerosol model parameters, including effective radius (r_{eff}), effective deviation (v_{eff}), and refractive indices (m_{r}, m_{i}) as listed in Table 3. The a priori knowledge of $\boldsymbol{b}$ is essential to provide certain auxiliary constraints on the rationality of the final solutions. For the fixed observation location of ground-based field tests in our research, the a priori knowledge adopted in the forward simulation and inversion is characterized by the aerosol properties in Table 2. To describe the wavelength-dependence of refractive indices, it is assumed that the parameters following the power–law relationship are adopted [22].

Table 3. Definition of the measurement vector and state vector.

Name	Setting
Measurement vector	$\boldsymbol{y} = [I_{490}, I_{550}, I_{670}, I_{870}, I_{1610}]^T$
Observation uncertainties	$\boldsymbol{S}_{\mathrm{y}} = \epsilon_I^2 \boldsymbol{I}^2(\lambda)$, ϵ_I = 5% (relative error)
State vector	$\boldsymbol{x} = [V_0, \mathrm{FMF_v}]^T$ $V_0 \geq 0.001\ \mu\mathrm{m}^3/\mu\mathrm{m}^2$ $0.01 \leq \mathrm{FMF_v} \leq 0.99$
A priori estimates uncertainties	$\boldsymbol{S}_{\mathrm{a}} = \begin{pmatrix} \epsilon_{V_0}^2 V_0^2 & 0 \\ 0 & \epsilon_{\mathrm{FMF_v}}^2 \mathrm{FMF_v}^2 \end{pmatrix}$ $\epsilon_{V_0} = 100\%$, $\epsilon_{\mathrm{FMF_v}} = 100\%$ (relative error)

3. Experimental Data

As one of the most polluted regions affected by anthropogenic aerosol emissions, Beijing, the capital of China, is an area where there is deep concern about particulate pollution [49,50]. Thus, the field experiment was performed in Beijing from November 2–November 15, 2017. In order to compare and validate with AERONET observations, the experiment location was next to the AERONET Beijing_RADI site. Figure 2 shows the variations of AOD and $PM_{2.5}$ (with unit of $\mu g/m^3$) during the experiment. The AOD and $PM_{2.5}$ data were from AERONET and the Beijing Municipal Environmental Protection Monitoring Center (BMEMC), respectively. From Figure 2, we can see that Beijing experienced several haze events. The mean AOD on November 6 and 9 was about 1.4, representing a high pollution situation, while the mean AOD on November 3 and 10 was about 0.1, which represents clean atmospheric conditions. A good consistency between AOD and $PM_{2.5}$ was found when AOD was less than 0.4, while for high pollution conditions, there were relatively larger differences between AOD and $PM_{2.5}$. Furthermore, the weather conditions were very suitable for testing the proposed algorithms.

With regard to the measuring instrument, we adopted the newly developed Synchronization Monitoring Atmospheric Corrector (SMAC) sensor. SMAC is a satellite instrument designed to provide aerosol and cloud properties for the atmospheric corrections of a high-resolution camera onboard the same satellite. In order to achieve this purpose, the sensor has a total of eight channels from

blue (490 nm) through to near-infrared (1610 and 2250 nm). The observations included intensity bands centered at 490, 550, 670, 870, 1610, and 2250 nm, and four of these bands had polarimetric measurement capabilities, except for channel 550 nm (the polarization measurements were not used in this paper). There were also two channels centered at 910 and 1380 nm for water vapor remote sensing, where major water vapor absorption bands were located. The bandwidth was between 20 and 60 nm, depending on the spectral bands. Furthermore, the single-viewing sensor had a high time resolution of up to 10 samplings per second. In the experiment, continuous zenith observations were conducted, and all the measurements were carried out under cloudless conditions. Since the detectors in the 2250 nm channel needed to be passively cooled, and were difficult to achieve a stable operating temperature, the data on that wavelength were not available for ground-based measurements. Figure 3 shows the measurements of sky light by SMAC at 490, 550, 670, 870, and 1610 nm on November 6, 2017. The horizontal axis is the UTC time (from 1–8, corresponding to Beijing time 9 a.m.–4 p.m.), and the ordinate axis is the radiance. From Figure 3, the sky light radiance gradually increased with the solar zenith angle, reached the maximum at midday, and then gradually decreased.

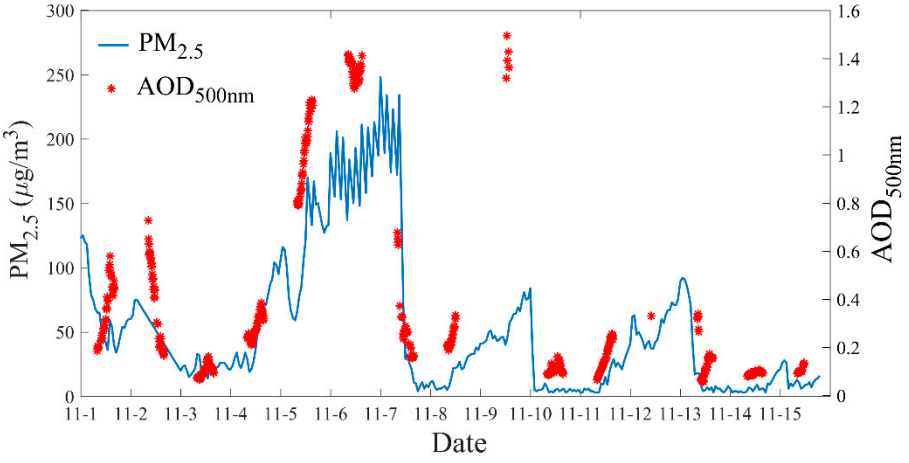

Figure 2. The aerosol optical depth (AOD) and $PM_{2.5}$ (particulate matter with aerodynamic diameter less than 2.5 μm) during the field experiment. The AOD data are from the aerosol robotic network (AERONET) Beijing_RADI site, and the $PM_{2.5}$ data are from the Beijing Municipal Environmental Protection Monitoring Center.

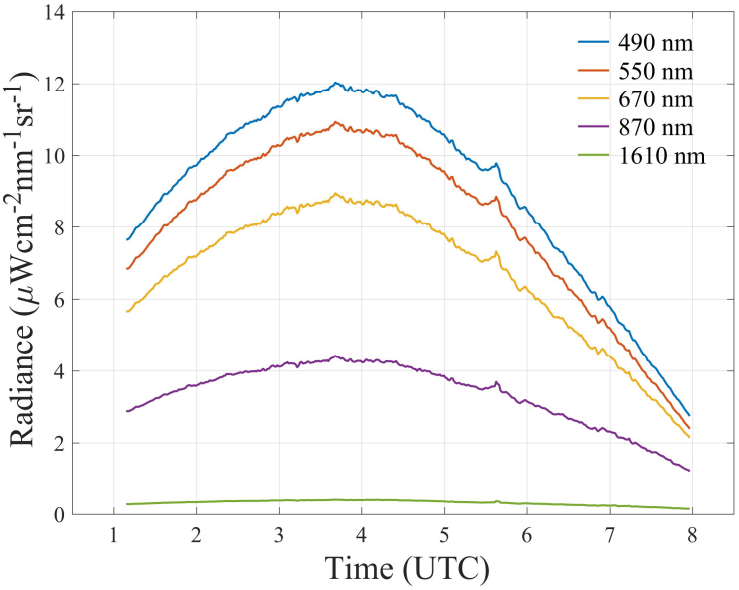

Figure 3. Measurement data of the field experiments located in Beijing (6 November 2017).

4. Results

4.1. Retrieval from Synthetic Data

For the proposed OE-based algorithm, we paid attention to three issues: The dependence on a priori assumptions, the measurement error influence, and the reliability of the aerosol model parameters [51]. Among these three aspects, if reasonable a priori estimates and a priori knowledge are available, observation error is the main source that affects the inversion accuracy. Thus, with the support of relatively accurate a priori knowledge from AERONET products, we mainly made a test on the inversion algorithm by introducing various observation errors. The purpose was to verify the stability of the inversion algorithm and the confidence in the retrieved results.

Firstly, simulations of sky scattering radiation measurements were performed by UNL-VRTM. The viewing geometries, including solar zenith angle (SZA), view zenith angle (VZA), and relative azimuth angle (RAA), are listed in Table 4. Different aerosol AOD from 0.1–3.0, with FMF_o varying from 0.1–0.95, were considered in the simulation. Secondly, to simulate the measurement error, a 5% relative noise following a Gaussian distribution was introduced to the simulation results. After that, the optimal estimation retrieval was performed on the synthetic data superimposed with noise.

Table 4. The parameter settings for the simulation of analog data.

Parameters	Setting
Solar zenith angle (SZA)	60°
View zenith angle (VZA)	0° (vertical upward observation)
Relative azimuth angle (RAA)	0° (solar principal plane)
Aerosol optical depth (AOD) at 550 nm	from 0.1–3.0
Fine-mode fraction (FMF_o) at 550 nm	from 0.1–0.95

Figure 4 shows the scatterplots between the inversion results and the true value at 550 nm. The left panel represents the scenario without noise, and the right panel represents the scenario with 5% random noise. The correlation coefficients in the left panel were both greater than 0.99, which indicated a good self-consistency of the OE algorithm. As seen in Figure 4b, the uncertainty of the retrieved AOD increased significantly with the aerosol loading. The mean inversion error was about 4.5% when AOD was less than 2.0, while the mean inversion error was up to 7.76% when AOD was greater than 2.0. As seen in Figure 4d, the mean inversion error of FMF_o was 4.36%. Evidently, the aerosol retrieval from a single-viewing observation was susceptible to measurement error. Even so, the uncertainties of the inversion results were of the same order of magnitude as the observation uncertainties. In summary, the developed algorithm showed good performance, regardless of the high aerosol loading situation.

The simulated radiances, cost function, and gradient vector for each iteration during the retrieval progress are shown in Figure 5. Four cases at different aerosol loadings (AOD = 0.2 and AOD = 1.0 at 550 nm) and fine-mode fraction (FMF_o = 0.2 and FMF_o = 0.8) were selected, in which FMF_o = 0.2 and FMF_o = 0.8 represented coarse-dominated and fine-dominated aerosol, respectively. As seen in Figure 5a, the model results gradually approached the true value with the iteration. A more than 99% reduction in cost function was achieved, as seen in Figure 5b,c. The Gradient of V_0 and FMF_v approached zero after convergence, as shown in Figure 5d. The details of the inversion process indicated that the OE algorithm had good performance in obtaining the optimal results. Furthermore, the single-viewing multi-spectral observations provided sufficient information to contain the retrieval of FMF_v theoretically.

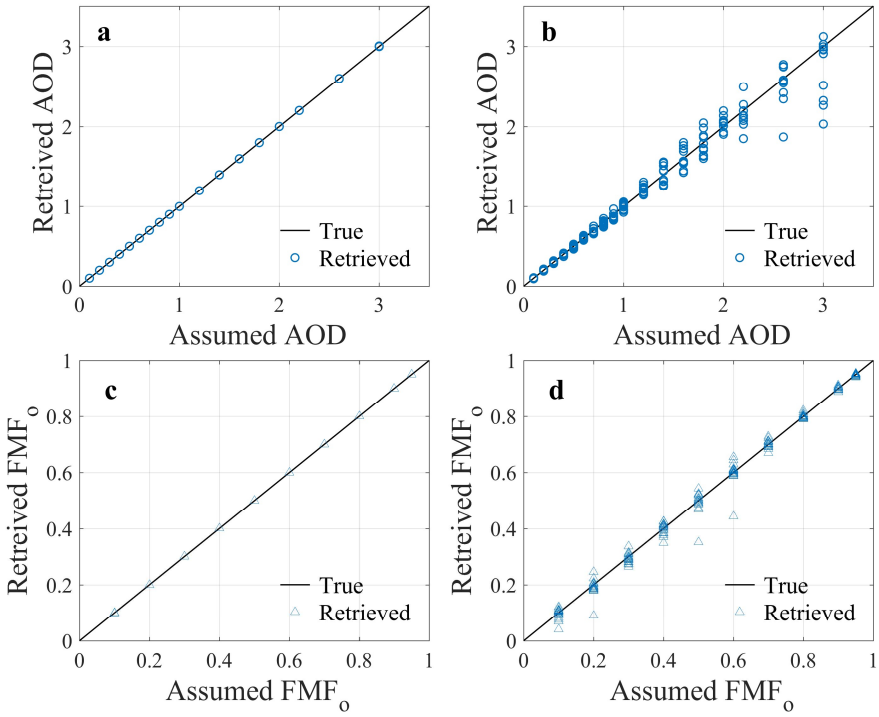

Figure 4. The scatter plot between retrieved results and true values at 550 nm, for eighteen different aerosol loadings from AOD = 0.1 to 3.0 and ten different mixed states from FMF_o = 0.1 to 0.95. (**a**) and (**c**) in left panel represents retrieval of V_0 and FMF_o without observation noise added. (**b**) and (**d**) in right panel represents retrieval of V_0 and FMF_o with 5% random noise added.

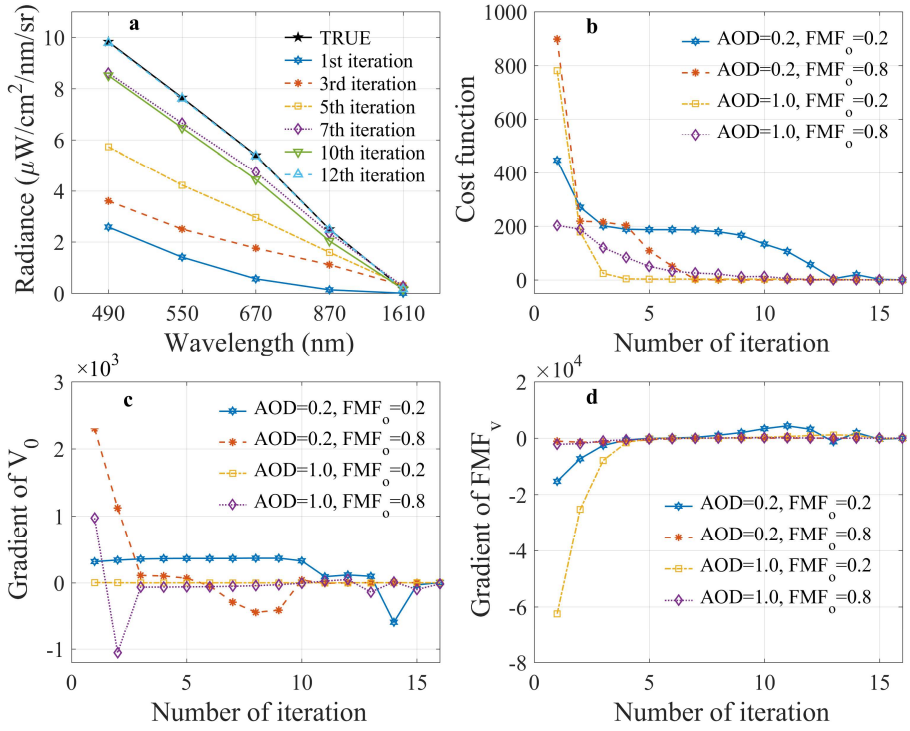

Figure 5. Illustration of the iterative process. (**a**) plots the simulated radiances of the five wavelengths at each iteration and the true radiances under the condition of AOD = 1.0 and FMF_o = 0.8 at 550 nm. (**b**) plots the cost function as a function of the number of iterations under four different conditions. (**c**) and (**d**) are the gradient vectors of V_0 and FMF_v, respectively.

4.2. Retrieval from Experimental Data

4.2.1. Validation of V_0 and FMF_v

Furthermore, the OE-based algorithm was performed on the experimental data. The validation of V_0 and FMF_v against AERONET inversion products are shown in Figure 6. For an accurate comparison, the SMAC observation time was limited to a range of ±15 min based on the AERONET sky radiation measurement time. As seen in the left panel of Figure 6, data from 490 and 670 nm channels were used for the inversion. As seen in the middle panel, data from four channels (490, 550, 670, and 870 nm) were used for inversion, while in the right panel, the channel of 1610 nm was introduced for the retrieval. In regard to V_0, the correlation coefficients (R) were 0.90, 0.95, and 0.98 for the three scenarios, respectively. Correspondingly, the root-mean-square-error ($RMSE$) were 0.296, 0.089, and 0.041, respectively. Likewise, the R values were 0.838, 0.897, and 0.939, while the $RMSE$ were 0.101, 0.074, and 0.057 for each of the three FMF_v scenarios, respectively. The results clearly showed a good performance of our algorithm. It can be seen from Figure 6f that the retrieval of FMF_v was significantly improved since the observation of the 1610 nm wavelength provided extra information on coarse-mode aerosol. Consequently, the inversion accuracy of FMF_v was further improved. However, the deviations of FMF_v were larger than total volume, which means that there were still some uncertainties in retrieving FMF_v. On one hand, the AERONET inversion algorithm adopted multi-angle sky light observations, combined with precise direct AOD measurements, which provided sufficient information to constrain the multi-parameter retrieval of aerosol, including the PSD parameters. While the proposed algorithm in this paper used single-viewing measurements, and the aerosol PSD model parameters were considered as a priori knowledge rather than as state vectors. Consequently, the a priori estimation might have affected the validation results. On the other hand, the calibration error of the SMAC instrument might have been another important factor. A previous study showed that for the OE inversion framework, the observation error was the main factor influencing the uncertainties of the inversion results [52].

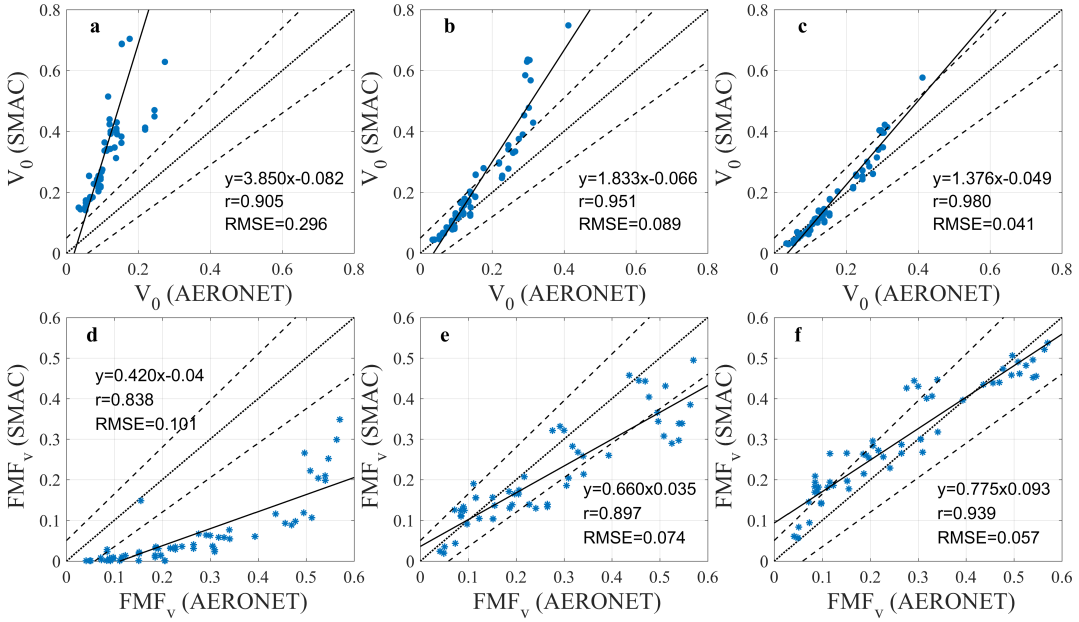

Figure 6. The scatter plot of retrieved V_0 (upper panel) and FMF_v (lower panel) compared to the AERONET inversion products. (**a**) and (**d**) denote the scenarios of two channels (490, 670 nm). (**b**) and (**e**) denote the scenarios of four channels (490, 550, 670, and 870 nm). (**c**) and (**f**) denote the scenarios of all the five intensity channels (including 1610 nm), respectively. The solid line, dotted line, and dashed line represent the fit line, 1:1 line, and the expected error line ($\Delta x = \pm 0.05 \pm 0.15x$), respectively.

4.2.2. Validation of AOD and FMF_o

The spectral AOD and FMF_o retrieved synchronously by the OE algorithm were compared to AERONET AOD (direct solar products) and FMF (spectral deconvolution algorithm (SDA) products), separately. For the validation, the SMAC observation time was limited to the range of ±1 min, based on the AERONET measurement time.

In Figure 7a, the *R*-value for AOD at 500 nm was 0.99, while the *RMSE* was 0.1, which represented good AOD retrieval results. However, the slope of the fit line was 1.16, which indicated that the retrieved AOD is larger than AERONET AOD in highly polluted conditions. For the validation of FMF_o in Figure 7b, the *R*-value and *RMSE* were 0.948 and 0.099, respectively. However, it is worth noting that the slope of the fit line had a relatively low value of 0.59. The results showed a strong correlation while suffering from a positive bias. In other words, there was an overestimate of fine-mode aerosol and an underestimate of coarse-mode aerosol. In this regard, our results were consistent with the work of O'Neil et al. [20]. Such results were caused by the difference in definition and acquisition methods. Moreover, the validation of AE was also performed, as shown in Figure 7c. As seen in Figure 7c, there was a positive bias in retrieved AE value, and the bias decreased gradually as the AE value increased. The AE value was inversely related to the average size of the particles in the aerosol; the smaller the particles, the larger the exponent. Thus, the validation results were consistent with Figure 7b, which indicated either more fine-mode particles related to the coarse-mode particles, or smaller radius fine-mode particles. In general, there was a slight system offset between the retrieved results from SMAC and the direct solar products. There may have been two reasons for the offset. One was due to the applicability of aerosol model parameters at high AOD conditions, and the other comes from the SMAC calibration errors.

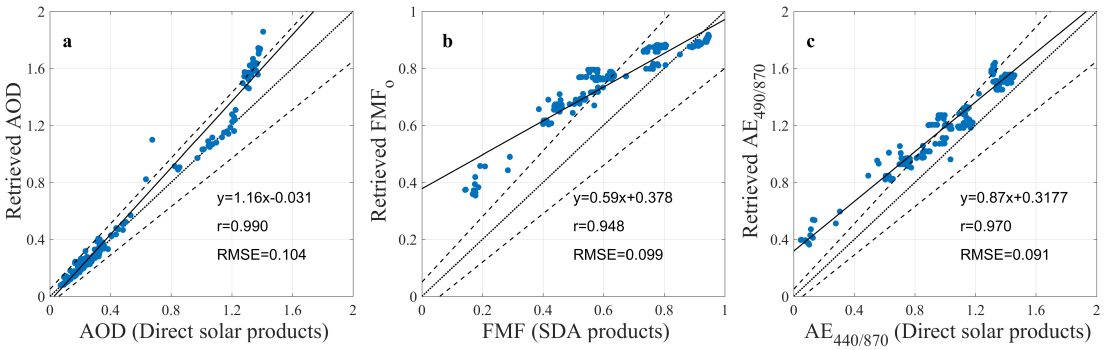

Figure 7. The scatter plot of retrieved (**a**) AOD at 500 nm, (**b**) FMF_o at 500 nm, and (**c**) Ångström Exponent compared to the AERONET direct solar products. The solid line, dotted line, and dashed line represent the fit line, 1:1 line, and the expected error line ($\Delta x = \pm 0.05 \pm 0.15x$), respectively.

4.2.3. Fitting Residuals

The OE inversion algorithm finds the best fit between the forward simulations and measurements at all of the wavebands. The disagreement between the measurements and the simulations with best inversion results can be characterized by the fitting residual, which is defined as,

$$\delta(\lambda) = (I_{\text{fit}}(\lambda) - I_{\text{meas}}(\lambda))/I_{\text{meas}}(\lambda). \quad (12)$$

The spectral residual errors are the mean value of $\delta(\lambda)$ for all measurement data. Although there were slight differences between different measurement channels, we set the same weighting in the retrieval. Therefore, when the cost function reached a minimum value, the fitting residuals were not the same at different wavelengths. The spectral residual errors were 9.28%, 1.45%, 8.14%, 4.42%, and 1.46% for 490, 550, 670, 870, and 1610 nm, respectively. Obviously, the errors for 490 and 670 nm were much larger than the other wavelengths, due to the calibration error and the forward model error in these

wavelengths. The total residual error was the average of the five wavebands, which was as low as 4.95%, showing a good fit between the final model results and the real observations.

5. Discussion

5.1. The Limit of the Algorithm

The OE-based algorithm takes advantage of the effective information in longer NIR band observations to enhance the constraints of coarse-mode aerosol inversion. Thus, the FMF parameter can be retrieved from single-viewing observation. However, after introducing 5% random noise on the simulation data, the mean relative retrieval error was about 4.5%, which revealed the relative low ability of error resistance for the single-viewing observation.

The real part of the refractive index and the effective radius are two decisive parameters in the optical scattering characteristics of aerosol, and they further affect the retrieval of FMF. In this study, we use the historical statistical data from AERONET products in the experimental area as the a priori estimates of aerosol model parameters. However, for practical applications, different aerosol types need to be considered.

5.2. Application Potential

The algorithm proposed originally for ground-based intensity measurements is based on the optimal estimation inversion theory. Thus, it can be extended conveniently by adjusting the observation vector for other applications as long as the observations contain sufficient information. Polarimetry is one of the most prospective remote sensing approaches since it has a high sensitivity to aerosol [25]. SMAC also provides polarimetric measurements. Research on aerosol retrieval from the polarization data based on the proposed algorithm can be conducted. Furthermore, by introducing appropriate surface estimation methods, the algorithm can be further used for satellite platforms. Based on the feasibility of remote sensing FMF from ground-based single-viewing multi-spectral observation, a further inversion study for satellites can be carried out. The proposed algorithm is expected to be applied to aerosol remote sensing of SMAC on board the Chinese HJ-02 satellite in the future.

6. Conclusions

In this paper, we proposed an optimal estimation inversion algorithm for the retrieval of the aerosol fine-mode fraction parameter from single-viewing multi-spectral measurements of sky light. The retrieved AOD and FMF from synthetic data produced a correlation coefficient greater than 0.99, representing good self-consistency of the inversion algorithm. Validation against the AERONET products showed that the correlation coefficients for aerosol volume fine-mode fraction (FMF_v) and optical fine-mode fraction (FMF_o) were 0.94 and 0.95, respectively. The mean residual error of all the retrieval data was 4.95%. These results strongly validate the feasibility of the inversion framework. In addition, by introducing data from the 1610 nm wavelength measurements, the correlation coefficients showed a significant improvement for FMF_o (from 0.89–0.94). The comparison confirms the expected high value of NIR data to the retrieval of the aerosol fine-mode fraction.

Author Contributions: X.S. and Z.L. conceived of and designed the experiments. Y.M. and Y.F. performed the field experiments; K.L. and L.L. assisted with the data analyzing and preprocessing. W.H. guided the optimal estimation method and revised the paper; F.Z. conducted the algorithm operation and wrote the paper; J.H. and Y.Q. provided technical guidance and useful advice regarding the calibration of raw data.

Funding: This study is support by the National Key R&D Program of China (grant number 2016YFE0201400), the Open Fund of the State Key Laboratory of Remote Sensing Science (grant number OFSLRSS201710), and the National Natural Science Foundation of China (grant numbers 41871269, 41671367, 41701407, 41505022).

Acknowledgments: We are very grateful to Jun Wang and Xiaoguang Xu for the UNL-VRTM code. The data and Fortran codes used for the forward simulations are available at the link in the website (http://www.unl-vrtm.org). We also acknowledge the L-BFGS-B software package developed by Ciyou Zhu, Jorge Nocedal, and Richard Byrd.

Conflicts of Interest: The authors declare no conflict of interest.

References

1. Dockery, D.W.; Rd, P.C.; Xu, X.; Spengler, J.D.; Ware, J.H.; Fay, M.E.; Ferris, B.G., Jr.; Speizer, F.E. An association between air pollution and mortality in six U.S. Cities. *New Engl. J. Med.* **1993**, *329*, 1753–1759. [CrossRef] [PubMed]
2. Kaufman, Y.J.; Boucher, O.; Tanré, D.; Chin, M.; Remer, L.A.; Takemura, T. Aerosol anthropogenic component estimated from satellite data. *Geophys. Res. Lett.* **2005**, *32*, 317–330. [CrossRef]
3. Hoek, G.; Krishnan, R.M.; Beelen, R.; Peters, A.; Ostro, B.; Brunekreef, B.; Kaufman, J.D. Long-term air pollution exposure and cardio- respiratory mortality: A review. *Environ. Health* **2013**, *12*, 43. [CrossRef] [PubMed]
4. Cohen, A.J.; Brauer, M.; Burnett, R.; Anderson, H.R.; Frostad, J.; Estep, K.; Balakrishnan, K.; Brunekreef, B.; Dandona, L.; Dandona, R. Estimates and 25-year trends of the global burden of disease attributable to ambient air pollution: An analysis of data from the global burden of diseases study 2015. *Lancet* **2017**, *389*, 1907–1918. [CrossRef]
5. Seaton, A.; Godden, D.; Macnee, W.; Donaldson, K. Particulate air pollution and acute health effects. *Lancet* **1995**, *345*, 176–178. [CrossRef]
6. Song, C.; He, J.; Wu, L.; Jin, T.; Chen, X.; Li, R.; Ren, P.; Zhang, L.; Mao, H. Health burden attributable to ambient $PM_{2.5}$ in china. *Environ. Pollut.* **2017**, *223*, 575. [CrossRef]
7. Zhang, Y.; Li, Z. Remote sensing of atmospheric fine particulate matter ($PM_{2.5}$) mass concentration near the ground from satellite observation. *Remote Sens. Environ.* **2015**, *160*, 252–262. [CrossRef]
8. Li, Z.; Zhang, Y.; Shao, J.; Li, B.; Hong, J.; Liu, D.; Li, D.; Wei, P.; Li, W.; Li, L.; et al. Remote sensing of atmospheric particulate mass of dry $PM_{2.5}$ near the ground: Method validation using ground-based measurements. *Remote Sens. Environ.* **2016**, *173*, 59–68. [CrossRef]
9. Li, Z.; Wei, Y.; Zhang, Y.; Xie, Y.; Li, L.; Li, K.; Ma, Y.; Sun, X.; Zhao, W.; Gu, X. Retrieval of atmospheric fine particulate density based on merging particle size distribution measurements: Multi-instrument observation and quality control at shouxian. *J. Geophys. Res. Atmos.* **2018**, *123*, 12–474. [CrossRef]
10. Yan, X.; Shi, W.Z.; Li, Z.Q.; Li, Z.Q.; Luo, N.N.; Zhao, W.J.; Wang, H.F.; Yu, X. Satellite-based $PM_{2.5}$ estimation using fine-mode aerosol optical thickness over china. *Atmos. Environ.* **2017**, *170*, 290–302. [CrossRef]
11. Zhang, Y.; Li, Z.; Qie, L.; Zhang, Y.; Liu, Z.; Chen, X.; Hou, W.; Li, K.; Li, D.; Xu, H. Retrieval of aerosol fine-mode fraction from intensity and polarization measurements by parasol over east asia. *Remote Sens.* **2016**, *8*, 417. [CrossRef]
12. Kaufman, Y.J.; Wald, A.E.; Remer, L.A.; Bo-Cai, G.; Rong-Rong, L.; Flynn, L. The modis 2.1-µm channel-correlation with visible reflectance for use in remote sensing of aerosol. *IEEE Trans. Geosci. Remote Sens.* **1997**, *35*, 1286–1298. [CrossRef]
13. Levy, R.C.; Remer, L.A.; Mattoo, S.; Vermote, E.F.; Kaufman, Y.J. Second-generation operational algorithm: Retrieval of aerosol properties over land from inversion of moderate resolution imaging spectroradiometer spectral reflectance. *J. Geophys. Res. Atmos.* **2007**, *112*. [CrossRef]
14. Levy, R.C.; Remer, L.A.; Kleidman, R.G.; Mattoo, S.; Ichoku, C.; Kahn, R.; Eck, T.F. Global evaluation of the collection 5 modis dark-target aerosol products over land. *Atmos. Chem. Phys.* **2010**, *10*, 10399–10420. [CrossRef]
15. Zhao, A.; Li, Z.; Zhang, Y.; Zhang, Y.; Li, D. Merging modis and ground-based fine mode fraction of aerosols based on the geostatistical data fusion method. *Atmosphere* **2017**, *8*, 117. [CrossRef]
16. Dubovik, O.; Herman, M.; Holdak, A.; Lapyonok, T.; Tanré, D.; Deuzé, J.L.; Ducos, F.; Sinyuk, A.; Lopatin, A. Statistically optimized inversion algorithm for enhanced retrieval of aerosol properties from spectral multi-angle polarimetric satellite observations. *Atmos. Meas. Tech.* **2011**, *4*, 975–1018. [CrossRef]
17. Waquet, F.; Cornet, C.; Deuzé, J.L.; Dubovik, O.; Ducos, F.; Goloub, P.; Herman, M.; Lapyonok, T.; Labonnote, L.C.; Riedi, J.; et al. Retrieval of aerosol microphysical and optical properties above liquid clouds from polder/parasol polarization measurements. *Atmos. Meas. Tech.* **2013**, *6*, 991–1016. [CrossRef]
18. Zhang, Y.; Li, Z.; Qie, L.; Hou, W.; Liu, Z.; Zhang, Y.; Xie, Y.; Chen, X.; Xu, H. Retrieval of aerosol optical depth using the empirical orthogonal functions (eofs) based on parasol multi-angle intensity data. *Remote Sens.* **2017**, *9*, 578. [CrossRef]

19. Lolli, S.; Madonna, F.; Rosoldi, M.; Campbell, J.R.; Welton, E.J.; Lewis, J.R.; Gu, Y.; Pappalardo, G. Impact of varying lidar measurement and data processing techniques in evaluating cirrus cloud and aerosol direct radiative effects. *Atmos. Meas. Tech.* **2018**, *11*, 1639–1651. [CrossRef]
20. O'Neill, N.T.; Eck, T.F.; Smirnov, A.; Holben, B.N.; Thulasiraman, S. Spectral discrimination of coarse and fine mode optical depth. *J. Geophys. Res. Atmos.* **2003**, *108*. [CrossRef]
21. Holben, B.N.; Eck, T.F.; Slutsker, I.; Tanré, D.; Buis, J.P.; Setzer, A.; Vermote, E.; Reagan, J.A.; Kaufman, Y.J.; Nakajima, T.; et al. Aeronet—A federated instrument network and data archive for aerosol characterization. *Remote Sens. Environ.* **1998**, *66*, 1–16. [CrossRef]
22. Dubovik, O.; King, M.D. A flexible inversion algorithm for retrieval of aerosol optical properties from sun and sky radiance measurements. *J. Geophys. Res. Atmos.* **2000**, *105*, 20673–20696. [CrossRef]
23. Knobelspiesse, K.; Cairns, B.; Mishchenko, M.; Chowdhary, J.; Tsigaridis, K.; Van, D.B.; Martin, W.; Ottaviani, M.; Alexandrov, M. Analysis of fine-mode aerosol retrieval capabilities by different passive remote sensing instrument designs. *Opt. Express* **2012**, *20*, 21457–21484. [CrossRef]
24. Li, Z.; Hou, W.; Hong, J.; Zheng, F.; Luo, D.; Wang, J.; Gu, X.; Qiao, Y. Directional polarimetric camera (dpc): Monitoring aerosol spectral optical properties over land from satellite observation. *J. Quant. Spectrosc. Radiat. Transf.* **2018**, *218*, 21–37. [CrossRef]
25. Dubovik, O.; Li, Z.; Mishchenko, M.I.; Tanr¨¦, D.; Karol, Y.; Bojkov, B.; Cairns, B.; Diner, D.J.; Espinosa, W.R.; Goloub, P.; et al. Polarimetric remote sensing of atmospheric aerosols: Instruments, methodologies, results, and perspectives. *J. Quant. Spectrosc. Radiat. Transf.* **2019**, *224*, 474–511. [CrossRef]
26. Kokhanovsky, A.A. The modern aerosol retrieval algorithms based on the simultaneous measurements of the intensity and polarization of reflected solar light: A review. *Front. Environ. Sci.* **2015**, *3*, 4. [CrossRef]
27. Li, Z.Q.; Xu, H.; Li, K.T.; Li, D.H.; Xie, Y.S.; Li, L.; Zhang, Y.; Gu, X.F.; Zhao, W.; Tian, Q.J.; et al. Comprehensive study of optical, physical, chemical, and radiative properties of total columnar atmospheric aerosols over china: An overview of sun–sky radiometer observation network (sonet) measurements. *Bull. Am. Meteorol. Soc.* **2018**, *99*, 739–755. [CrossRef]
28. Hou, W.; Li, Z.; Wang, J.; Xu, X.; Goloub, P.; Qie, L. Improving remote sensing of aerosol microphysical properties by near-infrared polarimetric measurements over vegetated land: Information content analysis. *J. Geophys. Res. Atmos.* **2018**, *123*, 2215–2243. [CrossRef]
29. Rodgers, C.D. *Inverse Methods for Atmospheric Sounding: Theory and Practice*; World Scientific: Singapore, 2000.
30. Waquet, F.; Cairns, B.; Knobelspiesse, K.; Chowdhary, J.; Travis, L.D.; Schmid, B.; Mishchenko, M.I. Polarimetric remote sensing of aerosols over land. *J. Geophys. Res. Atmos.* **2009**, *114*. [CrossRef]
31. Xu, X.; Wang, J.; Zeng, J.; Spurr, R.; Liu, X.; Dubovik, O.; Li, L.; Li, Z.; Mishchenko, M.I.; Siniuk, A.; et al. Retrieval of aerosol microphysical properties from aeronet photopolarimetric measurements: 2. A new research algorithm and case demonstration. *J. Geophys. Res. Atmos.* **2015**, *120*, 7079–7098. [CrossRef]
32. Xu, X.; Wang, J.; Henze, D.K.; Qu, W.; Kopacz, M. Constraints on aerosol sources using geos-chem adjoint and modis radiances, and evaluation with multisensor (omi, misr) data. *J. Geophys. Res. Atmos.* **2013**, *118*, 6396–6413. [CrossRef]
33. Anderson, T.L.; Wu, Y.; Chu, D.A.; Schmid, B.; Redemann, J.; Dubovik, O. Testing the modis satellite retrieval of aerosol fine-mode fraction. *J. Geophys. Res. Atmos.* **2005**, *110*. [CrossRef]
34. Anderson, T.L.; Masonis, S.J.; Covert, D.S.; Ahlquist, N.C.; Howell, S.G.; Clarke, A.D.; Mcnaughton, C.S. Variability of aerosol optical properties derived from in situ aircraft measurements during ACE-Asia. *J. Geophys. Res. Atmos.* **2003**, *108*. [CrossRef]
35. Kleidman, R.G.; O'Neill, N.T.; Remer, L.A.; Kaufman, Y.J.; Eck, T.F.; Tanré, D.; Dubovik, O.; Holben, B.N. Comparison of moderate resolution imaging spectroradiometer (modis) and aerosol robotic network (aeronet) remote-sensing retrievals of aerosol fine mode fraction over ocean. *J. Geophys. Res. Atmos.* **2005**, *110*. [CrossRef]
36. Zhang, Y.; Li, Z.; Zhang, Y.; Li, D.; Qie, L.; Che, H.; Xu, H. Estimation of aerosol complex refractive indices for both fine and coarse modes simultaneously based on aeronet remote sensing products. *Atmos. Meas. Tech.* **2017**, *10*, 3203–3213. [CrossRef]
37. Liu, Z.; Mortier, A.; Li, Z.; Hou, W.; Goloub, P.; Lv, Y.; Chen, X.; Li, D.; Li, K.; Xie, Y. Improving daytime planetary boundary layer height determination from caliop: Validation based on ground-based lidar station. *Adv. Meteorol.* **2017**, *2017*, 1–14. [CrossRef]

38. Zhang, W.; Guo, J.; Miao, Y.; Liu, H.; Zhang, Y.; Li, Z.; Zhai, P. Planetary boundary layer height from caliop compared to radiosonde over china. *Atmos. Chem. Phys.* **2016**, *16*, 9951–9963. [CrossRef]
39. Wang, J.; Xu, X.; Ding, S.; Zeng, J.; Spurr, R.; Liu, X.; Chance, K.; Mishchenko, M. A numerical testbed for remote sensing of aerosols, and its demonstration for evaluating retrieval synergy from a geostationary satellite constellation of geo-cape and goes-r. *J. Quant. Spectrosc. Radiat. Transf.* **2014**, *146*, 510–528. [CrossRef]
40. Xu, X.; Wang, J. Retrieval of aerosol microphysical properties from aeronet photopolarimetric measurements: 1. Information content analysis. *J. Geophys. Res. Atmos.* **2015**, *120*, 7059–7078. [CrossRef]
41. Hou, W.; Wang, J.; Xu, X.; Reid, J.S.; Han, D. An algorithm for hyperspectral remote sensing of aerosols: 1. Development of theoretical framework. *J. Quant. Spectrosc. Radiat. Transf.* **2016**, *178*, 400–415. [CrossRef]
42. Hou, W.; Wang, J.; Xu, X.; Reid, J.S. An algorithm for hyperspectral remote sensing of aerosols: 2. Information content analysis for aerosol parameters and principal components of surface spectra. *J. Quant. Spectrosc. Radiat. Transf.* **2017**, *192*, 14–29. [CrossRef]
43. Hou, W.Z.; Li, Z.Q.; Zheng, F.X.; Qie, L.L. Retrieval of aerosol microphysical properties based on the optimal estimation method: Information content analysis for satellite polarimetric remote sensing measurements. In *ISPRS - International Archives of the Photogrammetry, Remote Sensing and Spatial Information Sciences*; 2018; pp. 533–537.
44. Luenberger, D.G.; Ye, Y. Linear and nonlinear programming. *Int. Encycl. Soc. Behav. Sci.* **2004**, *67*, 8868–8874.
45. Yu, J.; Li, M.; Wang, Y.; He, G. A decomposition method for large-scale box constrained optimization. *Appl. Math. Comput.* **2014**, *231*, 9–15. [CrossRef]
46. Zhu, C.; Byrd, R.H.; Lu, P.; Nocedal, J. A Limited Memory Fortran Code for Solving Bound Constrained Optimization Problems. *Technique Report, Northwestern Univ.* **1994**.
47. Byrd, R.H.; Lu, P.; Nocedal, J.; Zhu, C. A limited memory algorithm for bound constrained optimization. *SIAM J. Sci. Comput.* **1995**, *16*, 1190–1208. [CrossRef]
48. Xiao, Y.; Zhang, H. Modified subspace limited memory bfgs algorithm for large-scale bound constrained optimization. *J. Comput. Appl. Math.* **2008**, *222*, 429–439. [CrossRef]
49. Che, H.; Xia, X.; Zhu, J.; Wang, H.; Wang, Y.; Sun, J.; Zhang, X.; Shi, G. Aerosol optical properties under the condition of heavy haze over an urban site of beijing, china. *Environ. Sci. Pollut. Res.* **2015**, *22*, 1043–1053. [CrossRef] [PubMed]
50. Ou, Y.; Zhao, W.H.; Wang, J.Q.; Zhao, W.J.; Zhang, B. Characteristics of aerosol types in beijing and the associations with air pollution from 2004 to 2015. *Remote Sens.* **2017**, *9*, 19. [CrossRef]
51. Torres, B.; Dubovik, O.; Fuertes, D.; Schuster, G.; Cachorro, V.E.; Lapyonok, T.; Goloub, P.; Blarel, L.; Barreto, A.; Mallet, M.; et al. Advanced characterisation of aerosol size properties from measurements of spectral optical depth using the grasp algorithm. *Atmos. Meas. Tech.* **2017**, *10*, 3743–3781. [CrossRef]
52. Zheng, F.; Hou, W.; Li, Z. Optimal estimation retrieval for directional polarimetric camera onboard chinese gaofen-5 satellite: An analysis on multi-angle dependence and a posteriori error. *Acta Phys. Sin.* **2019**, *68*, 40701.